


# Carrier trapping centers in a two-dimensional silica bilayer: Strongly localized shallow gap states and resonances induced by oxygen vacancies

Nestor Fajardo  and Ricardo Wagner Nunes <sup>\*</sup>

*Departamento de Física, Universidade Federal de Minas Gerais, Belo Horizonte, Minas Gerais, Brazil*

 (Received 6 May 2022; revised 11 August 2022; accepted 27 September 2022; published 18 October 2022)

Structural and electronic properties of neutral native defects in a two-dimensional SiO<sub>2</sub> bilayer (2D-SiO<sub>2</sub>) are examined using the SIESTA *ab initio* approach. We identify scissor and rotation modes of oxygen atoms, in the middle of Si-O-Si chains, as low-energy structural excitations responsible for the response of the 2D-SiO<sub>2</sub> lattice to the formation of all native defects in the present study. Furthermore, we find that oxygen native defects (single vacancies and interstitials) should be the most abundant defect species in thermal-equilibrated samples. Regarding native-defect electronic states, single oxygen vacancies and interstitials are found to be amphoteric trapping centers in 2D-SiO<sub>2</sub>. Silicon vacancies and interstitials introduce several strongly localized states spanning a large fraction of the gap. Generally, we identify a marked tendency for the appearance of strongly spatially localized defect states, be their energies shallow or deep within the band gap, as well as the emergence of strongly localized resonances in the valence and/or conduction bands. Strong spatial localization of defect states, a hallmark of systems displaying trapping and polaronic effects, is a result of quantum confinement and enhanced Coulombic effects in this 2D system. Carrier trapping and polaron formation are thus expected to be a common feature of defect states and added carriers in 2D-SiO<sub>2</sub>.

DOI: [10.1103/PhysRevB.106.155416](https://doi.org/10.1103/PhysRevB.106.155416)

## I. INTRODUCTION

Stackings of two-dimensional (2D) materials that interact through van der Waals interactions (usually called van der Waals stackings) are the current paradigm for the investigations of prospective electronic devices built from 2D materials, because they offer the possibility of modulating the electronic and structural properties of the ensuing materials along the stacking direction.

Over the last decade, SiO<sub>2</sub> has been synthesized in 2D forms (2D-SiO<sub>2</sub>) [1–4], with potential applications as a highly permselective membrane and also as a prototype material where the glass transition can be directly observed [5]. This 2D-SiO<sub>2</sub> bilayer is the thinnest possible system with SiO<sub>2</sub> stoichiometry that is fully chemically saturated, i.e., devoid of dangling bonds. It interacts weakly with the substrates on which it is grown, via van der Waals interactions [1].

Being the thinnest possible chemically saturated SiO<sub>2</sub> layer, and a mechanically and chemically stable van der Waals-interacting 2D material with an experimental band gap of 6.7 eV [1], the most important prospective application of a 2D-SiO<sub>2</sub> bilayer should be as an ultrathin insulating layer in van der Waals stackings.

As in most of the three-dimensional (3D) polymorphs of silica, 2D-SiO<sub>2</sub> is built from a structural motif of corner-sharing tetrahedra, where oxygen atoms in each of the four shared vertices are bonded to two silicon atoms in the centers of adjoining tetrahedra, resulting in a SiO<sub>2</sub> stoichiometry. In the case of 2D-SiO<sub>2</sub>, this motif is structured as a bilayer con-

sisting of two mirror-image layers of SiO<sub>2</sub> tetrahedra sharing an oxygen layer in the middle. Oxygens in this middle layer sit on the vertices shared by the mirror-image tetrahedra from the “top” and “bottom” external layers, as shown in Fig. 1. On the two external layers, each oxygen atom sits on a vertex shared by two adjoining tetrahedra.

Systematic investigation of the fundamental physical properties of silicate-based 3D compounds have been of paramount importance in the development of silicon-based technology, ranging from fiber optics to semiconductor devices. In the solid form, three-dimensional SiO<sub>2</sub> (3D-SiO<sub>2</sub>) appears in several crystalline phases such as  $\alpha$  quartz and  $\beta$  quartz, among others, and also in amorphous phases such as natural silica, glass, and opal. Most of these 3D solids consist of networks of the aforementioned structural motif of corner-sharing tetrahedra.

Experimental and theoretical studies of the properties of native defects and impurities in the 3D-SiO<sub>2</sub> polymorphs have a long history, and a large body of work on the topic is available in the literature [6–14]. We mention explicitly here only previous studies that are directly related to our results for native defects in the crystalline form of 2D-SiO<sub>2</sub>.

The predominant native defect in 3D-SiO<sub>2</sub> is the oxygen vacancy, which is regarded as the culprit behind the degradation of SiO<sub>2</sub>-based electronic devices [15,16]. Experimentally, it is well established [6,8,9] that the most frequent O-vacancy defect in quartz is the so-called  $E'$  EPR center, with an unpaired electron ( $S = 1/2$ ), but an  $E''$  center with two unpaired electrons in a triplet ( $S = 1$ ) state has also been reported [9]. In amorphous 3D-SiO<sub>2</sub> (a-SiO<sub>2</sub>), an  $E_\delta$  defect shows an EPR profile very similar to that of the  $E'$  center. Both  $E'$  and  $E_\delta$  have been assigned to the positively charged O

<sup>\*</sup>rwnunes@fisica.ufmg.br

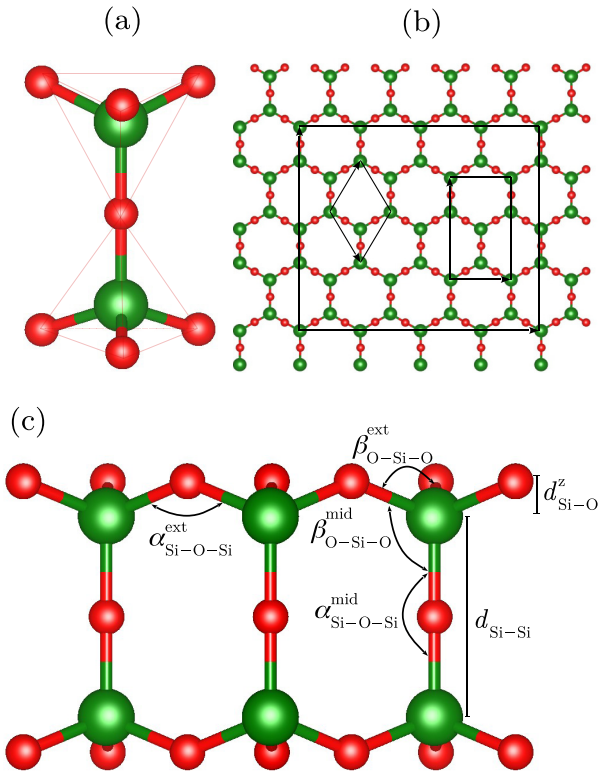


FIG. 1. Atomic structure of a 2D-SiO<sub>2</sub> bilayer. (a) Side view of the structural motif of mirror-image tetrahedra sharing a vertex. Oxygen atoms (red spheres) sit on the vertices and silicon atoms (green spheres) at the center of each tetrahedron. (b) Top view of the 2D-SiO<sub>2</sub> bilayer. Si atoms form top and bottom AA-stacked honeycomb sublattices with an O atom in the middle of Si-O-Si links. The diamond-shaped primitive 12-atom cell, a rectangular 24-atom unit cell, and the 192-atom [(4 × 2) × the rectangular unit cell] supercell used in most of our calculations are indicated by black lines. (c) Side view showing the structural parameters of the 2D-SiO<sub>2</sub> bilayer. Definitions and values of the bond angles and bond lengths shown in the figure are included in Table I.

vacancy, based on theoretical *ab initio* calculations [16]. A more recent first-principles study [17,18] suggests that Si<sub>2</sub> dimers could be responsible for an unidentified paramagnetic center in vitreous 3D-SiO<sub>2</sub> (v-3D-SiO<sub>2</sub>). By examining nondimer configurations in positively charged states, these authors consider puckered, unpuckered, doubly puckered, and forward-oriented configurations and find that the calculated EPR parameters of the puckered and unpuckered configurations support the assignment of an  $E'_g$  center in v-3D-SiO<sub>2</sub> to an unpaired spin localized at a threefold-coordinated silicon dangling bond. Moreover, the forward-oriented configurations are suggested as the assignment of an  $E'_g$  center in v-3D-SiO<sub>2</sub>.

A feature of oxygen vacancies in the 3D polymorphs of SiO<sub>2</sub> that deserves mention, in the context of the present work, is the bistability of this defect in  $\alpha$  quartz: in the neutral state, the O vacancy is stable in a dimer configuration, where a Si-Si bond is formed between the two Si dangling bonds that appear due to the removal of the O atom, while in the positively charged state the defect assumes the so-called puckered configuration, where one of the Si atoms relaxes across the

plane of its other three oxygen nearest neighbors and bonds with another O atom in the 3D network, to restore its fourfold coordination [9,10,16].

Overall, several experimental studies have addressed defects associated with oxygen and silicon vacancies in 3D-SiO<sub>2</sub>, and have found that the latter appears mostly in quartz crystallized at relatively low temperature (<250 °C) from amorphous silica precursors due to rapid cooling [19–21].

The 3D polymorphs of SiO<sub>2</sub> are prone to carrier trapping and polaron formation. Intrinsic (involving polaron formation) and extrinsic (involving Ge or Li impurities) electron-trapping phenomena have been investigated using *ab initio* methods in  $\alpha$  quartz and amorphous SiO<sub>2</sub> [22,23].

In the case of 2D crystals, an issue that requires attention in the context of defect states is the influence of quantum confinement and enhanced Coulombic effects on the character of the wave function of the electronic states introduced in the fundamental band gap (and possibly strongly localized resonances and antiresonances in the valence and conduction bands) by native defect and impurities. Regarding the issue of enhanced Coulombic effects, it is well known that, often, exciton binding energies in lower-dimensional systems are one to two orders of magnitude larger than in 3D crystals [24,25].

The current work is a systematic theoretical investigation of the electronic structure and atomic geometry of native defects (single vacancies and interstitials), in crystalline 2D-SiO<sub>2</sub>. We consider a freestanding 2D-SiO<sub>2</sub> bilayer; i.e., effects of interaction with the substrate are not accounted for in our calculations.

A previous work on defects in the 2D-SiO<sub>2</sub> bilayer [26] has considered only the fully reconstructed topological lattice defects, in the form of non-hexagonal rings that appear in amorphous 2D-SiO<sub>2</sub> (a-2D-SiO<sub>2</sub>) and in defects such as the Stone-Wales defect and the double vacancy in the crystalline form. These are defects with a similar morphology to that observed for the same type of defects in graphene [27–31]. In this work, we consider single vacancies and interstitials, with a morphology that is markedly different from similar defects in graphene.

We employ the SIESTA-code implementation [32] of Kohn-Sham density functional theory (KS-DFT) [33,34] to address the electronic structure and atomic geometry of neutral native defects in crystalline 2D-SiO<sub>2</sub>. The work is a first exploratory step toward addressing the properties of native-defect and impurity states in a system that is bound to become relevant for the foreseeable applications of 2D semiconductors and insulators, given its central role in “traditional” 3D-materials electronic devices.

As such, we employ the Perdew-Burke-Ernzerhof (PBE) generalized gradient approximation (GGA) functional to describe exchange and correlation effects [35]. It is well known that the GGA approximation underestimates the band gaps of semiconductors and insulators, but it turns out that in the case of 2D-SiO<sub>2</sub> this is not too severe an issue, because the GGA-calculated band gap of 5.6 eV that we obtain in our calculations is underestimated by 16% only, when compared with recent experimental values of 6.7 eV. As discussed in the following, with this computational scheme we obtain a description of the structural features of the pristine bulk of

2D-SiO<sub>2</sub> in excellent agreement with available experimental results.

Our calculations for the electronic structure of the pristine bulk of 2D-SiO<sub>2</sub> show that at  $-1.73$  eV below the top of the valence bands there emerges a very strong van Hove singularity, associated with a set of flat valence bands in this energy range, that should give rise to a strong peak in the ultraviolet absorption signal of a 2D-SiO<sub>2</sub> layer. No such strong electronic singularity is observed in the 3D forms of 3D-SiO<sub>2</sub>.

We address the properties of four native defects in the neutral charge state in 2D-SiO<sub>2</sub>: single O and Si vacancies,  $V_O$  and  $V_{Si}$ , and single O and Si interstitials,  $I_O$  and  $I_{Si}$ . In order to examine the thermodynamic stability of these native defects, we consider a range of chemical potential values for silicon and oxygen, from Si-rich conditions to O-rich conditions.

Generally, in our study oxygen native defects are found to be the most abundant species in thermal equilibrated samples, under the synthesis conditions encoded in our choices of chemical potentials. Oxygen vacancies are more stable in the intermediate layer of O atoms than in the external layers, by 0.44 eV, the opposite being true for the oxygen interstitials, which are much more stable in the external layer, by 2.27 eV, than in the intermediate layer. Overall, the middle-layer oxygen vacancy is the most stable defect over the first three-fifths of the range of chemical potentials we consider, starting from the Si-rich limit, and the external-layer oxygen interstitial becomes the most stable defect from there up to the O-rich limit.

Regarding defect atomic structure, our calculations show that the response of the atomic lattice to the presence of the native defects is dominated by two types of displacements of the O atoms in the middle of the Si-O-Si chains: (i) a rotation mode, where oxygen atoms rotate about the axis joining the two Si atoms; and (ii) scissor-mode displacements that change the angle at the O vertex in a Si-O-Si chain. Rotation and scissor modes are found to be low-energy structural excitations of the 2D-SiO<sub>2</sub> atomic lattice, and constitute the mechanism by which this system responds to the formation of all native defects in the present study. The two honeycomb sublattices of Si atoms remain nearly unaffected by the presence of the defects, except at the very core of the defect, in all cases. In a forthcoming publication, we will discuss the ubiquitous role of these structural modes in the response of the 2D-SiO<sub>2</sub> lattice to external stresses and deformations.

In the main text, we provide a detailed analysis of the electronic states introduced in the fundamental band gap of 2D-SiO<sub>2</sub> by each native defect in our study. A general trend we identify in the present work is a tendency, across all defect species we consider, for the formation of strongly localized defect levels, be their energy shallow or deep within the band gap. Another trend we identify is the formation of localized states that are resonant within the bulk bands, near the edges of the valence and/or conduction bands.

More specifically, both oxygen monovacancies and single interstitials are found to be amphoteric trapping centers in 2D-SiO<sub>2</sub>. In the case of the O vacancy, activation of donor or acceptor states depends on whether the vacant site is on one of the external layers or in the middle oxygen layer. Single O interstitials display acceptor and donor levels in both stable positions we identify in our calculations.

Our results indicate that in 2D-SiO<sub>2</sub>, even shallow defect states may commonly exhibit strongly localized wave functions, and trapping and polaronic effects may be a more common feature of defect states in 2D-SiO<sub>2</sub> than in 3D-SiO<sub>2</sub>, as a result of quantum confinement and enhanced Coulombic effects in 2D systems.

We plan to revisit the main results of this work with calculations employing hybrid and GGA +  $U$  functionals in a forthcoming publication. A natural next step for our investigations of 2D-SiO<sub>2</sub> is to address the problem of charged defects, such that stable charge states and related transition levels are identified. A proper description of the fundamental band gap is an essential step in such study. While in 3D-SiO<sub>2</sub>, inclusion of a Hubbard- $U$  term has been found to correct the band gap only partially, from 40% underestimated within GGA to 33% within GGA +  $U$  [36], no such study has been performed in the case of the 2D form of SiO<sub>2</sub>. Given that we find the gap underestimated by 16% only within GGA, inclusion of a Hubbard- $U$  term may prove enough to fully fix “the gap problem” and allow an accurate prediction of the transition levels in this material.

Another extension of the present work that we plan to undertake in the future is the first-principles calculation of defect migration barriers of the native defects we consider in the present work. While *ab initio* molecular dynamics (MD) may also be considered in the context of defect migration in this system, migration barriers of the fully reconstructed defects involve covalent-bond breaking and tend to be quite high, which renders *ab initio* MD quite prohibitive in these cases. In the partially reconstructed defects, that show dangling bonds at the core of the defect, the lubrication of the migration pathway by the dangling bonds [37] may allow *ab initio* MD to provide useful insight on the migration path in these cases. To our knowledge, so far MD dynamics has been applied only to model the ring statistics of the amorphous form of 2D-SiO<sub>2</sub> [38–42].

## II. METHODOLOGY

In our *ab initio* calculations, we have employed DFT in the Kohn-Sham framework, as implemented in the SIESTA software [32]. In order to model the structural and electronic properties of the pristine 2D-SiO<sub>2</sub> bilayer, a 12-atom primitive cell was used, with tight convergence parameters to obtain well converged structural properties, band structure, and density of states: a mesh cutoff of 800 Ry, with a  $128 \times 128 \times 1$  Monkhorst-Pack (MP) grid [43], and a Gaussian smearing of 0.01 eV to draw curves for the density of states (DOS) and orbital-projected DOS (PDOS). For the structural relaxation of internal parameters, a tolerance on the residual forces of  $\leq 0.001$  eV/Å was imposed. All calculations in this work were performed using the experimental lattice constant of 5.42 Å, obtained by LEED, STM, and AFM measurements on ordered films of 2D-SiO<sub>2</sub> grown on Ru(0001) substrates [1,44].

For the calculations of the properties of native defects, very good convergence with respect to supercell size was obtained with 192-atom supercells, except for the case of the external-layer oxygen vacancy, that required a 432-atom supercell in order to avoid spurious overlap between the defect states and their periodic images. For the self-consistency of



the electronic charge density and the convergence of structural parameters, a  $2 \times 2 \times 1$  MP  $k$ -point grid and a mesh cutoff of 250 Ry were used in the 192-atom-supercell calculations, and a  $\Gamma$ -point sampling was used for the 432-atom calculation. In all supercell calculations, tolerance of  $\leq 0.01$  eV/Å was imposed on the residual forces in every atom. In order to obtain well converged DOS and PDOS for the defect supercells, MP grids of  $16 \times 16 \times 1k$  points were employed. In all cases, a double- $\zeta$  pseudoatomic basis set augmented with polarization orbitals (DZP basis) was employed, with an energy cutoff of 0.01 Ry, and the PBE-GGA functional to account for exchange and correlation effects [35]. Interactions between valence electrons and ionic cores were described by Troullier-Martins pseudopotentials [45]. Spin polarization was considered in all cases.

In what follows, we discuss the spatial distribution of the electronic states that appear in the band gap due to the formation of each native defect we consider. We also discuss some examples of resonances that appear in the valence and conduction bands. We propose a simple scheme [46] to analyze the spatial structure of the defect-state wave functions, based on the orbital-projected density of states, that is described in detail in the Supplemental Material [54]. In a few words, we analyze the PDOS to quantify and add up the contributions of the atomic-basis orbitals of each atom to the defect states (and resonances, in some cases), and plot this as a function of the distance of the atom from the defect center. We refer to these defect-state plots as the wave-function spatial profile,  $P_{wf}(R)$ .

With this simple scheme, we can distinguish between gap states and resonances that are very strongly localized, usually within  $\sim 5$  Å from the defect center, and effective-mass-theory (EMT) states that show weaker exponential decay. EMT states, which are the standard description of shallow doping gap states in 3D crystals, are more delocalized, extending over a much larger portion of the lattice, away from the defect center. Furthermore, plots of isosurfaces of the charge density of the defect-state wave functions are also analyzed.

### III. STRUCTURAL AND ELECTRONIC PROPERTIES OF A CRYSTALLINE 2D-SiO<sub>2</sub> BILAYER

#### A. Structural parameters

The equilibrium structure of crystalline 2D-SiO<sub>2</sub> is a bilayer composed of two (top and bottom) mirror-image external layers, with nominal Si<sub>2</sub>O<sub>3</sub> stoichiometry, sharing an intermediate (or middle) layer of oxygen atoms. Oxygen atoms in the middle layer are bonded to two Si atoms, one directly above it in the top layer and another directly below it in the bottom layer, resulting in the overall SiO<sub>2</sub> stoichiometry, as shown in Fig. 1. The Si atoms in each of the two external layers form AA-stacked honeycomb structures, with one oxygen atom in the middle of each Si-O-Si link, forming oxygen external sublayers. Overall, the lattice structure of 2D-SiO<sub>2</sub> is a hexagonal lattice with 12 atoms per primitive cell, belonging to the  $D_{6h}$  symmetry group, the same as graphene. The resulting values from our *ab initio* calculations for the structural parameters shown in Fig. 1 are included in Table I. Si-O bonds involving a middle-layer O atom ( $d_{\text{Si-O}}^{\text{mid}} = 1.65$  Å) are slightly smaller than Si-O bonds involving an external-layer O atom

TABLE I. Geometric parameters of the structure of a 2D-SiO<sub>2</sub> bilayer. Distances in Å and angles in degrees. Available experimental values, in parentheses, are from Refs. [47,48].  $d_{\text{Si-Si}}$   $\equiv$  distance between the two external Si honeycomb layers.  $d_{\text{Si-O}}^{\text{ext}}$   $\equiv$  distance between nearest-neighbor Si and O atoms in the same external layer.  $d_{\text{Si-O}}^{\text{z}}$   $\equiv$  distance between Si and O sublayers in the same external layer.  $\alpha_{\text{Si-O-Si}}^{\text{ext}}$   $\equiv$  Si-O-Si angle at external-layer O atom vertex.  $\alpha_{\text{Si-O-Si}}^{\text{mid}}$   $\equiv$  Si-O-Si angle at intermediate-layer O atom vertex.  $\beta_{\text{O-Si-O}}^{\text{ext}}$   $\equiv$  tetrahedral O-Si-O angle involving external-layer O atoms.  $\beta_{\text{O-Si-O}}^{\text{mid}}$   $\equiv$  tetrahedral O-Si-O angle involving one middle-layer O atom.

$d_{\text{Si-Si}}$	$d_{\text{Si-O}}^{\text{ext}}$	$d_{\text{Si-O}}^{\text{z}}$		
3.30	1.67	0.58		
	(1.67 $\pm$ 0.08, 1.66 $\pm$ 0.06)	(0.55 $\pm$ 0.04)		
$\alpha_{\text{Si-O-Si}}^{\text{ext}}$	$\alpha_{\text{Si-O-Si}}^{\text{mid}}$	$\beta_{\text{O-Si-O}}^{\text{ext}}$	$\beta_{\text{O-Si-O}}^{\text{mid}}$	
139.6	180	108.8	110.2	
(140.5)	(180)	(109.4 $\pm$ 8.1, 110.1 $\pm$ 5.7)		

( $d_{\text{Si-O}}^{\text{ext}} = 1.67$  Å), both values being slightly larger than Si-O bonds in 3D  $\alpha$  quartz (1.61 Å). The tetrahedral O-Si-O angles involving one middle-layer O atom ( $\beta_{\text{O-Si-O}}^{\text{mid}} = 110.2^\circ$ ) are slightly larger than the O-Si-O angles with both O atoms on a external layer ( $\beta_{\text{O-Si-O}}^{\text{ext}} = 108.8^\circ$ ). The former (latter) are larger (smaller) than the ideal tetrahedral angle of  $109.5^\circ$  by  $0.7^\circ$  only. The Si-O-Si angle is  $\alpha_{\text{Si-O-Si}}^{\text{mid}} = 180^\circ$  for bonds joining Si atoms in the two sublayers, with an oxygen atom in the middle layer, and  $\alpha_{\text{Si-O-Si}}^{\text{ext}} = 139.6^\circ$  for the Si-O-Si bonds with the three atoms on the same external layer. The distance between the two Si honeycomb sublayers is 3.30 Å. On each external layer, the O-atom sublayer is at a distance of 0.58 Å from the Si sublayer. All structural values are in very good agreement with the scanning-tunneling-microscopy (STM) results from Ref. [48], also included in Table I.

#### B. Electronic structure

The band structure and DOS of 2D-SiO<sub>2</sub> are shown in Fig. 2. In the top we show the electronic bands in the  $(-11.7, 2.0)$  eV interval, with the DOS shown on the right. In the lower panels we show separately the DOS for the valence (left panel) and conduction bands (right panel) in the corresponding energy intervals, as well as the PDOS of the atomic orbitals that give significant contributions to the electronic bands shown in the figure.

Unlike the case of  $\alpha$  quartz, which has an indirect band gap (top of the valence band at the  $K$  and  $M$  points and bottom of the conduction band at the  $\Gamma$  point, in the Brillouin zone) [49], in 2D-SiO<sub>2</sub> we obtain a direct gap with the two band extrema at the  $\Gamma$  point. We recall that a transition from indirect to direct band gap, on going from the 3D to the 2D form, occurs also in the case of 2D hexagonal metal dichalcogenides [50,51].

The Kohn-Sham-GGA value we obtain for the fundamental band gap is 5.6 eV. An important difference we obtain, between the electronic bands of the 2D and 3D forms of SiO<sub>2</sub>, is the width of the highest part of the valence band, which is 3.2 eV in 3D  $\alpha$  quartz [49] and only 0.9 eV in 2D-SiO<sub>2</sub>, which is indicative of enhanced correlation effects in the 2D

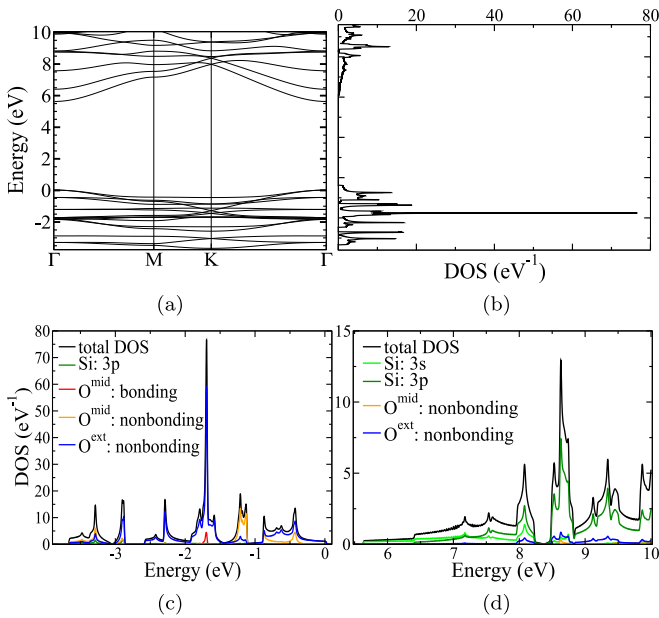


FIG. 2. (a) Band structure and (b) density of states (DOS) of a 2D-SiO<sub>2</sub> bilayer. (c) DOS and orbital-projected density of states (PDOS) of the valence bands. (d) DOS and PDOS of the conduction bands. In all panels, the zero of the energy scale is at the top of the valence band.

form. Moving down in energy in the valence band, this narrow band is followed by a pseudogap of  $\sim 0.2$  eV, related to a region populated solely by highly dispersive bands (hence the low DOS). Moving further down in energy, we find another rather narrow ( $\sim 0.3$  eV) set of bands followed by another pseudogap, and yet another narrow set of bands, with a width of  $\sim 1.2$  eV. In this latter set of bands, at  $-1.73$  eV below the top of the valence band ( $\epsilon_{vb}$ ), we observe a very strong van Hove singularity, associated with a set of flat bands in this energy range, that should give rise to a strong peak in the ultraviolet absorption signal of a 2D-SiO<sub>2</sub> layer. A true gap of  $\sim 0.3$  eV separates these bands from another set of bands, that display another pseudogap in their highest part.

The orbital composition of the valence bands, shown in Fig. 2(c) and Fig. 3(a), is similar to that of 3D-SiO<sub>2</sub>, being

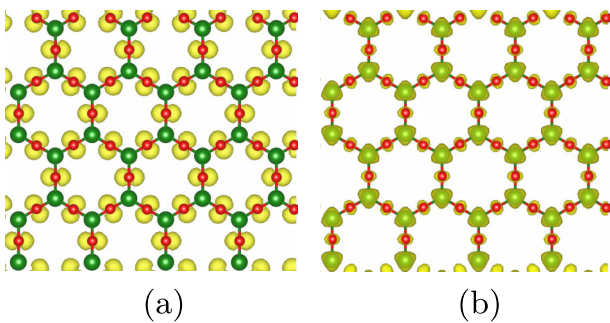


FIG. 3. Isosurfaces of charge density for bands at (a) the top of the valence band and (b) bottom of conduction band. The top of the valence band shows an orbital composition dominated by the nonbonding orbitals from oxygen atoms, while the bottom of the conduction band is composed mainly of silicon bonding orbitals.

mostly derived from the nonbonding orbitals of the oxygen atoms. The orbital character of the strong van Hove singularity is essentially the nonbonding orbitals of the oxygen atoms from the external layers, with a small contribution from bonding orbitals of the middle-layer O atoms. This is the only feature of the DOS of the three highest sets of valence bands that has some contribution from bonding oxygen orbitals. Note that, overall, Si orbitals give a negligible contribution to the valence bands.

Regarding the conduction bands, the scenario is also similar to quartz, with the conduction bands being derived primarily from the *s* and *p* orbitals of the Si atoms, as shown in Fig. 2(d) and Fig. 3(b), for an interval of  $\sim 2.4$  eV up from the bottom of the conduction band ( $\epsilon_{cb}$ ). States at the bottommost part of the conduction band are nearly entirely derived from the Si *s* orbitals, and the conduction bands remain mostly of *s* character up to  $\sim 1.7$  eV above  $\epsilon_{cb}$ . Moving up from this point, the states develop a predominant Si *p*-orbital character, with a progressively decreasing contribution of the Si *s* orbitals. Starting at  $\sim 2.4$  eV above  $\epsilon_{cb}$ , the nonbonding orbitals of the external-layer O atoms give a small but sizable contribution to the conduction-band states.

#### IV. NATIVE DEFECTS

In the Supplemental Material [54], for each native defect we analyze in the following, we include figures with detailed views of the atomic structure at the core of the defect, as well larger and more detailed figures of the DOS plots, the wavefunction spatial profiles, and isosurfaces of charge density of the defect states we discuss in the main text.

##### A. Vacancies

We start our discussion of native defects in crystalline 2D-SiO<sub>2</sub> by examining the energy levels and the spatial distribution of the defect states generated by O and Si vacancies. As described above, in a freestanding bilayer of crystalline 2D-SiO<sub>2</sub> there are two inequivalent O-atom positions: (i) an interlayer one, in the intermediate layer of oxygen atoms connecting a Si atom on the top external layer to a Si atom on the bottom external layer; (ii) an intralayer one, connecting two adjacent Si atoms on the same external Si honeycomb sublayer. In the case of Si, symmetry dictates that there is only one site, since all Si positions are symmetry related.

The defect levels of the three neutral vacancies are shown in Fig. 4. The labeling of the defects is as follows:  $V_O^{\text{mid}}$  is the interlayer oxygen vacancy that is formed by removing one oxygen atom from the middle (intermediate) layer.  $V_O^{\text{ext}}$  is the external-layer oxygen vacancy that is formed by removing one oxygen atom from either one of the two external layers.  $V_{Si}$  is a vacancy that is formed by removing a Si atom from either one of the two external layers.

##### 1. Middle-layer oxygen vacancy: $V_O^{\text{mid}}$

Let us first consider oxygen vacancies, the primary native defect center in crystalline and amorphous 3D-SiO<sub>2</sub> [9]. In the relaxed geometry of the  $V_O^{\text{mid}}$  defect, the local symmetry of the host lattice is only slightly broken at the defect site, due to small outward in-plane shifts of the three middle-layer O

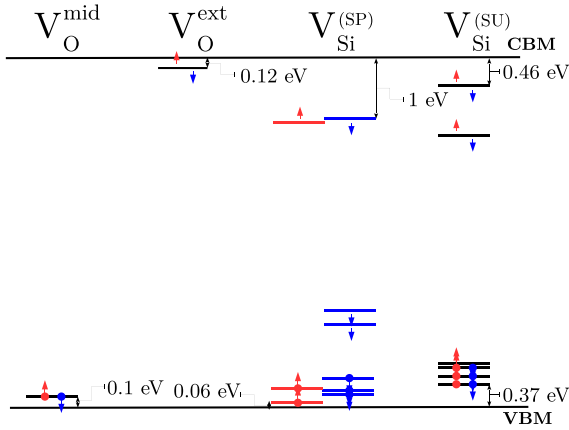


FIG. 4. Schematic representation of the single-particle energy levels introduced in the fundamental band gap by oxygen and silicon vacancies in 2D-SiO<sub>2</sub>.

atoms that are nearest to the vacant site, as shown in Figs. 5(a) and 5(b). Note that the top and bottom Si atoms, formerly bonded to the vacant O atom, move inward toward the middle layer and form a 2.39-Å-long interlayer bond, 0.91 Å shorter than the original Si-O-Si chain and only 1.6% larger than a Si-Si bond in the diamond-structure bulk of a Si crystal (2.35 Å). These two Si atoms at the defect core are shown as gray spheres in Figs. 5(c) and 5(d).

In Figs. 5(c) and 5(d), we show only the Si atoms in their positions in the V<sub>O</sub><sup>mid</sup> configuration. We draw lines joining the Si atoms (that do not represent real bonds in 2D-SiO<sub>2</sub>) to show that, after the removal of one middle-layer O atom, the lattice deforms very slightly and only in the very near vicinity of the

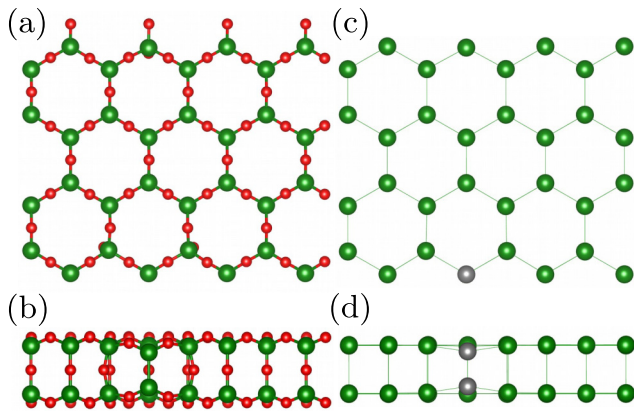


FIG. 5. Relaxed geometry of the middle-layer oxygen vacancy, V<sub>O</sub><sup>mid</sup>. (a) Top and (b) side views. Si (O) atoms are shown as green (red) spheres. (c) Top and (d) side views showing only the Si honeycomb sublattices. In (c) and (d), the two Si atoms that rebond at the defect core are shown as gray spheres, and the lines joining the Si atoms do not represent real bonds, and are drawn to show that the structure of the Si sublattices remains mostly undisturbed. In order to facilitate the visualization of the bond between the Si atoms shown as gray spheres, the supercell origin in all panels was chosen such as to show these Si atoms up front in the image. In Fig. 6(a), these two Si atoms are near the center of the supercell.

defect core, and that the local structure of the Si honeycomb sublattices is very much unaffected after relaxation of the atomic structure of the defect.

Thus, we observe that the response of the atomic lattice to the formation of the V<sub>O</sub><sup>mid</sup> defect consists essentially of two types of displacements of the O atoms in the middle of the Si-O-Si chains: (i) rotation about the axis joining the two Si atoms; (ii) displacements which change the angle at the O vertex in a Si-O-Si chain (a scissor mode). These rotation and scissor modes are low-energy structural excitations of the 2D-SiO<sub>2</sub> atomic lattice, and constitute the mechanism by which the 2D-SiO<sub>2</sub> lattice responds to the formation of all native defects in the present study. In a forthcoming publication, we will discuss the ubiquitous role of these structural modes in the response of 2D-SiO<sub>2</sub> lattice to external stresses and deformations.

This V<sub>O</sub><sup>mid</sup> defect geometry corresponds to the dimer configuration of O vacancies in 3D quartz and amorphous SiO<sub>2</sub>. We recall that in the crystalline forms of 3D-SiO<sub>2</sub>, positively charged O vacancies have another stable geometry, the so-called puckered configuration [9,10,16], where one of the Si atoms relaxes across the plane of its other three oxygen nearest neighbors and bonds with another O atom in the 3D network, to restore its fourfold coordination. In the 2D-SiO<sub>2</sub> case, no other layer of O atoms is available; hence this puckered configuration cannot exist, since upon puckering the Si atom would find the vacuum above (below) the top (bottom) layer.

Figure 4(a) shows the band edges of the conduction and valence bands and the singly degenerate shallow level, at  $\epsilon_{vb} + 0.10$  eV, that is introduced in the gap by the V<sub>O</sub><sup>mid</sup> defect in the neutral charge state. This level is fully occupied by two electrons with opposite spins; therefore V<sub>O</sub><sup>mid</sup> is EPR inactive in the neutral state.

Considering only the energy eigenvalue for this defect state, we would be tempted to classify it as, potentially, a shallow acceptor doping level. However, the wave function of this state, shown in Fig. 6(a), displays a fast exponential decay, and is very strongly localized on the atoms in the immediate vicinity of the vacant O-atom site: orbitals from the two silicon atoms, nearest neighbors to the vacant site, account for 33% of the DOS peak of the defect state, and the six nearest oxygen atoms (three on each of the two external layers) account for 51% of the defect-state DOS. Overall, the full wave function for the defect state is localized within  $\sim 5$  Å of the vacant site, as shown in Fig. 6(a). The inset in Fig. 6(a) shows an isosurface of the defect-state charge density, and provides another view of the strong localization of the shallow defect state. Therefore, despite being shallow in energy, the defect state is not an EMT state, and may act as a trapping center of carriers from the active layer in a prospective device employing 2D-SiO<sub>2</sub> as an insulating layer in a van der Waals stack.

This “pseudoshallow” V<sub>O</sub><sup>mid</sup> defect state underscores a fairly general trend that we observe in the present work: a marked prevalence for the formation of strongly localized defect levels, be their energy shallow or deep within the band gap. Another trend we identify is the formation of localized states that are resonant within the bulk bands, near the edges of the valence and/or conduction bands.



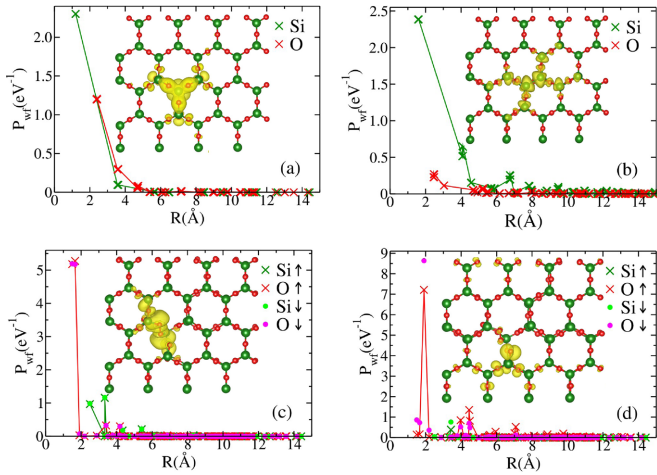


FIG. 6. (a) Wave-function spatial profile as a function of the distance to the defect center,  $P_{wf}(R)$ , of a strongly localized shallow defect state introduced in the band gap by the middle-layer oxygen vacancy,  $V_O^{mid}$ . (b)  $P_{wf}(R)$  of a strongly localized shallow defect state introduced in the band gap by the external-layer oxygen vacancy,  $V_O^{ext}$ . (c)  $P_{wf}(R)$  of the strongly localized spin-split pair of states introduced in the higher part of the band gap by the silicon vacancy,  $V_{Si}$ . Spin is indicated by arrows in the legend. The inset shows an isosurface of charge density of the majority-spin (spin-up) state. (d)  $P_{wf}(R)$  of the rather shallow  $V_{Si}$  majority-spin state, at  $\varepsilon_{vb} + 0.06$  eV, and of its spin-split minority-spin partner at  $\varepsilon_{vb} + 0.48$  eV. The inset shows an isosurface of charge density of the shallow state. In (a), (b), and (d) insets display isosurfaces of the charge density of the shallow states, as another view of their strongly spatially localized character. In all cases, contributions to  $P_{wf}(R)$  from Si (O) orbitals are shown as dark and light green (red and magenta) symbols and guide-to-the-eye lines.

In the case of  $V_O^{mid}$ , by zooming in on the electronic bands of the defect supercell, we identify three resonant states near the bottom of the conduction bands that are very strongly localized, within 4 Å from the defect center. The spatial localizations of the wave function of two of these resonances (the lowest and the highest in energy) are shown in Fig. S13 of the Supplemental Material [54]. The inset in this figure shows the bands for an interval of  $\sim 1.5$  from the bottom of the conduction band. The three resonant states are indicated by the red lines.

## 2. External-layer oxygen vacancy: $V_O^{ext}$

By removing an oxygen atom from either one of the external layers, the intralayer  $V_O^{ext}$  defect, shown in Figs. 7(a) and 7(b), is formed. Its relaxed geometry shows an intralayer Si-Si bond, with a 2.50 Å bond length replacing the Si-O-Si chain from which the O atom is removed. In this case also, the rotation and scissor modes of the O-atom sublattices dominate the response of the 2D-SiO<sub>2</sub> lattice to the introduction of the defect, and the symmetry of the Si sublattices is very nearly maintained, with a small symmetry reduction at the defect site due to the formation of the Si-Si bond, as shown in Figs. 7(c) and 7(d).

The  $V_O^{ext}$  defect is, in some respects, a reciprocal of the  $V_O^{mid}$ , in the sense that it introduces a singly degenerate

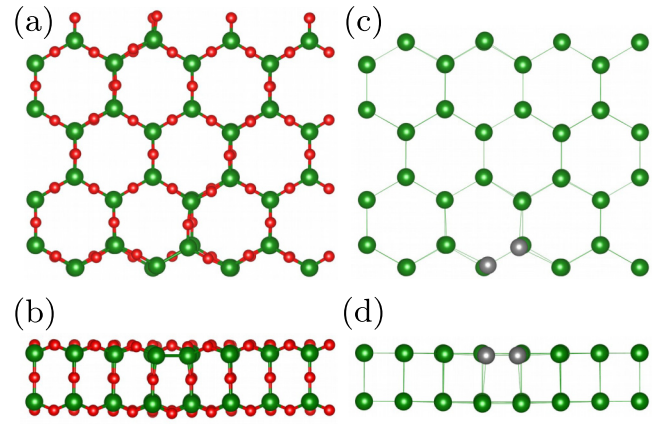


FIG. 7. Relaxed geometry of the external-layer oxygen vacancy,  $V_O^{ext}$ . (a) Top and (b) side views. Si (O) atoms are shown as green (red) spheres. (c) Top and (d) side views showing only the Si honeycomb sublattices; see caption in Fig. 5. In (c) and (d), the two Si atoms that rebond at the defect core are shown as gray spheres. In order to facilitate the visualization of the bond between the Si atoms shown as gray spheres, the supercell origin in all panels was chosen such as to show these Si atoms up front in the image. In Fig. 6(b), the two Si atoms are near the center of the supercell.

shallow defect state at  $\varepsilon_{cb} - 0.12$  eV. The defect level is empty in the neutral charge state of the defect; i.e., the neutral  $V_O^{ext}$  is also EPR inactive.

This is also a strongly localized pseudoshallow defect state, with most of its wave function concentrated on the orbitals of Si atoms within  $\sim 5$  Å of the vacant site. In this case,  $\sim 60\%$  of the defect-state wave function derives from the atomic orbitals of the two silicon atoms that rebond after the removal of the oxygen atom, the four nearest oxygen atoms, and the four next-nearest-neighbor silicon atoms, all in the same sublattice of the removed oxygen, as shown in Fig. 6(a). The figure shows the wave-function fast spatial decay and the inset shows an isosurface of charge density for this gap state.

Again, despite being shallow in energy, the  $V_O^{ext}$  state in the topmost part of the band gap is not an EMT state, and may trap electron carriers from the active layer in a prospective 2D-semiconductor device employing 2D-SiO<sub>2</sub> as an insulating layer. Also in this case we identify strongly localized resonances near the bottom of the conduction band, as shown in Fig. S16 of the Supplemental Material. That both oxygen vacancies display resonant states near the edge of the conduction band is related to the fact that a Si-Si bond is formed in the relaxed atomic structure of both defects, and the bottom of the conduction band derives entirely from Si orbitals.

From the above discussion, we conclude that oxygen monovacancies are amphoteric trapping centers in 2D-SiO<sub>2</sub>, with activation of the nominally donor or acceptor states depending on the Fermi level position and on whether the vacant site is on one of the external layers or in the middle oxygen layer.

Here, it is worth pausing to mention the work of Altman and Schwartz [52] where structural and electronic features of amorphous 2D-SiO<sub>2</sub> bilayers are observed directly with STM images at room temperature. While in the present work we do not consider a-2D-SiO<sub>2</sub> bilayers as in Ref. [52], these

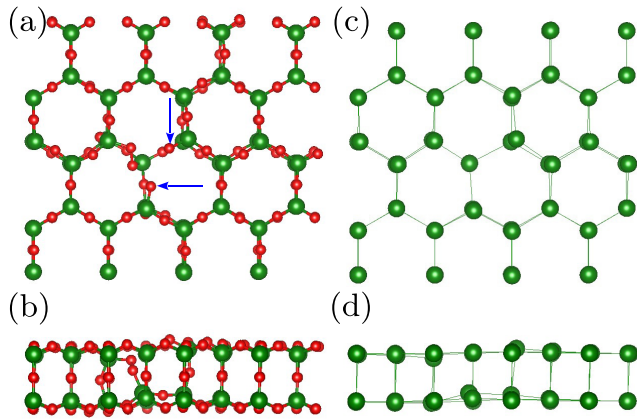


FIG. 8. Relaxed geometry of the silicon vacancy,  $V_{\text{Si}}$ . (a) Top and (b) side views. Si (O) atoms are shown as green (red) spheres. In (a) the blue arrows show the two undercoordinated O atoms in the core of the defect. (c) Top and (d) side views showing only the Si honeycomb sublattices; see caption in Fig. 5.

amorphous bilayers are also composed of two mirror layers of corner-sharing  $\text{SiO}_2$  tetrahedra, and show the same local bonding coordination of Si and O atoms. It is reasonable to expect that O vacancies should also be low-energy defects in a-2D- $\text{SiO}_2$  bilayers, with similar local geometric and electronic features such as the changes in the local density of states on the O-vacancy centers we identify in our calculations, and may be linked to the “fading wall” features of the STM images in Ref. [52].

### 3. Silicon vacancy: $V_{\text{Si}}$

As discussed below, a silicon vacancy  $V_{\text{Si}}$  is a high-formation-energy defect, markedly so in Si-rich growth conditions. However, one must bear in mind that irradiation with high-energy electron beams has been used to introduce carbon vacancies (also high-formation-energy defects) in graphene [53], and the same process may prove effective to engineer such defects in 2D- $\text{SiO}_2$ . Moreover, non-negligible concentrations of frozen-in Si vacancies result from rapid cooling of amorphous precursors, in 3D- $\text{SiO}_2$  samples [9].

Regarding the atomic structure, the relaxed geometry shows symmetry reduction over a somewhat larger portion of the surrounding lattice, when compared with  $V_{\text{O}}^{\text{mid}}$  and  $V_{\text{O}}^{\text{ext}}$ , and displays a partial reconstruction of the four broken bonds that appear due to the vacant Si atom. Figures 8(a) and 8(b) show the geometry of the partially reconstructed defect, after the removal of a Si from the top layer. As described above, in the pristine 2D- $\text{SiO}_2$  lattice each Si atom bonds to three O atoms in the same external sublayer and to one O atom in the intermediate layer. Upon removal of a Si atom, a bond is formed between an external layer O atom and the middle-layer O atom, such that a Si-O-O-Si chain is formed at the defect core, and each one of the other two external layer O atoms, formerly bonded to the vacant Si, are now undersaturated. The presence of O-atom dangling bonds, and the Si-O-O-Si bonding chain, not present in the host lattice, are the main reasons for the high formation energy of this defect.

Figures 8(c) and 8(d) show that even after the removal of a Si atom, substantial rebonding, and formation of the Si-O-O-Si chain, the two Si honeycomb sublattices are only mildly perturbed, being deformed more strongly only at the very core of the defect. Once again, we observe that in the relaxed geometry of the  $V_{\text{Si}}$  defect, besides the formation of the Si-O-O-Si chain, the scissor and rotation displacements of nearby O atoms constitute the mechanism by which the surrounding lattice responds to the perturbation.

Figure 4 shows the  $V_{\text{Si}}$  energy levels in the gap obtained from spin-unpolarized and spin-polarized calculations. The calculation without the inclusion of spin polarization yields five singly degenerate defect states introduced in the fundamental band gap by the  $V_{\text{Si}}$  defect, four of them in the lower half and one in the upper half of the band gap. In the neutral state of  $V_{\text{Si}}$ , the three lower levels are fully occupied with two electrons of opposite spins, and the two higher levels are empty. These defect states are composed essentially of atomic orbitals of the two undersaturated external-layer oxygen atoms (indicated by blue arrows in Fig. 8), and the atoms in the Si-O-O-Si chain at the core of the defect. In the spin-unpolarized calculation, all five gap states of the  $V_{\text{Si}}$  defect are very strongly localized in the immediate neighborhood of the defect center, regardless of being shallow or deep in the band gap.

From a spin-polarized calculation, the inclusion of exchange splitting has a dramatic effect. In the minority-spin channel, shown as blue lines in Fig. 4, we obtain three occupied and three unoccupied gap states, while the majority spin channel has only three energy levels in the band gap, two of which are occupied. The  $V_{\text{Si}}$  defect has a net spin of  $1 \mu_B$  (one Bohr magneton) in the neutral state.

In order to understand this defect-level structure, we must consider that spin splitting has pushed majority spin states downward, such that they become resonant within the valence band. The  $V_{\text{Si}}$  defect is a telling example of the occurrence of strongly localized defect-induced resonances in a 2D- $\text{SiO}_2$  bilayer. Below, we describe a spin-split pair consisting of a minority-spin gap state and a majority-spin valence-band resonance.

Overall, for the  $V_{\text{Si}}$  defect we have the following scenario:

(i) The two defect states with opposite spins in the higher part of the gap, in Fig. 4(c), result from a small spin splitting (72 meV) of the higher gap state from the spin-unpolarized calculation in Fig. 4(d). These states are composed essentially of orbitals from the two O and two Si atoms (predominantly from the O atoms) forming the Si-O-O-Si chain at the core of the defect. The wave-function spatial profiles for these defect states are shown in Fig. 6(c). They mirror each other and show strong localization near at defect core. The inset shows an isosurface of charge density for the majority-spin gap state, providing another perspective on its strong spatial localization.

(ii) The suite of four gap states spanning a small energy interval in the bottom part of the gap, from the spin unpolarized calculation, gives rise to complex effects of exchange spin splitting that push majority-spin states into the valence band as resonances and pulls one resonant minority-spin state from the valence band into the gap.



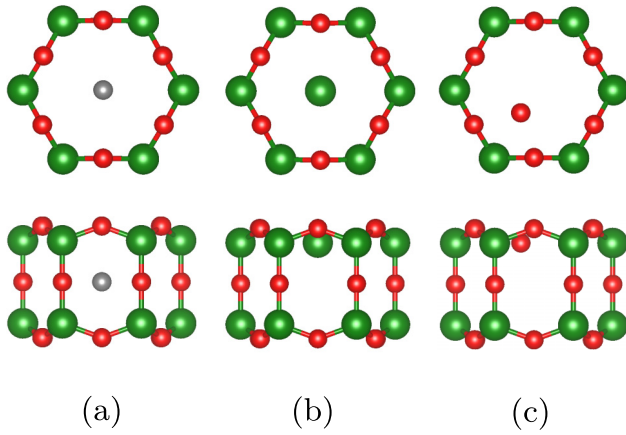


FIG. 9. Detail of the initial positions of interstitial atoms at the start of the geometry-relaxation procedure. The figure shows only the hexagon where the interstitial atom is initially placed, and not the full supercell. The relaxed-supercell atomic coordinates, in all cases, are included in the Supplemental Material. (a) Top and side views of the initial position of a Si or an O interstitial (gray sphere) in the middle layer. (b) Top and side views of the initial position of a Si interstitial in the external layer. (c) Top and side views of the initial position of an O interstitial in the external layer. Si (O) atoms are shown as green (red) spheres.

Figure 6(d) shows the wave functions of the rather shallow  $V_{\text{Si}}$  defect level, a majority-spin state with an energy of  $\varepsilon_{\text{vb}} + 0.06$  eV, and of its spin-split minority-spin partner at  $\varepsilon_{\text{vb}} + 0.48$  eV. Both states are composed mainly of the dangling bond orbitals of the O atom indicated by a blue horizontal arrow in Fig. 8. An isosurface of charge density for the shallow majority-spin state is shown in the inset. This is a prototype example of the tendency of formation of shallow states with strongly localized wave functions that we identify in the 2D-SiO<sub>2</sub> bilayer.

By examining the band structure of the defect supercell, we are able to identify a strongly localized majority-spin valence-band resonance at  $\varepsilon_{\text{vb}} - 0.20$  eV and its spin-split partner in the band gap, a minority spin state at  $\varepsilon_{\text{vb}} + 0.26$  eV, both states derived mainly from dangling bonds of the other under-coordinated O atom in the core of the  $V_{\text{Si}}$  defect, indicated by a blue vertical arrow in Fig. 8. The wave-function profiles for these spin-split partners and an isosurface of charge density for the minority-spin gap state are included in Fig. SI9 of the Supplemental Material [54]. Note that the resonant state does not decay to zero away from the defect center due to some degree of hybridization with the delocalized states in the valence band. Moreover, the spin-splitting energy is much larger for these latter spin-split pairs of states (0.42 and 0.46 eV) than for the states in the higher part of the gap.

## B. Interstitials

We shift gears now and consider single O and Si interstitials. Figure 9 shows the initial positions that we consider for an interstitial Si or O atom before geometry optimization: (a) an additional O (Si) atom placed on an interstitial site in the oxygen middle layer; (b) an additional Si atom placed at the

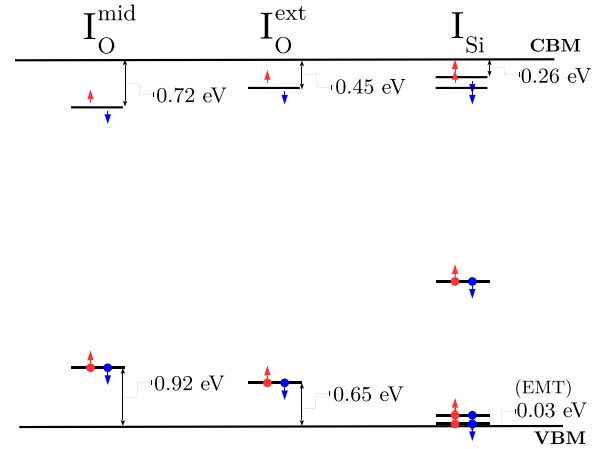


FIG. 10. Schematic representation of the single-particle energy levels introduced in the fundamental band gap by oxygen and silicon interstitials in 2D-SiO<sub>2</sub>.

center of an external-layer hexagon; (c) an additional O atom placed on an external-layer hexagon.

Oxygen atoms are usually stabilized in low-coordination environments, such as in 2D-SiO<sub>2</sub> where each O atom is twofold coordinated. As a result, from the initial positions described above we obtain two stable configurations of oxygen split interstitials in 2D-SiO<sub>2</sub>. On the other hand, Si atoms prefer higher coordination environments, and for that reason, in the case of a single Si interstitial, we obtain only one equilibrium position where the Si atom moves inward and bonds with the nearest O atom in the middle layer, for both initial positions shown in Fig. 9. We emphasize that even when initially placed on the external layer, an interstitial Si atom migrates to the middle layer and bonds with the closest middle-layer O atom, the driving force being the low coordination of available external-layer sites that renders the puckered configuration of the oxygen vacancy unstable in 2D-SiO<sub>2</sub>, as discussed above.

The defect levels introduced in the fundamental band gap by the three interstitial species are shown in Fig. 10. Below, we discuss the geometry and electronic structure of each case separately.

### 1. Oxygen split interstitials: $I_{\text{O}}^{\text{ext}}$ and $I_{\text{O}}^{\text{mid}}$

For both initial positions that we consider, after relaxation the interstitial O atom forms split interstitials in Si-O-O-Si chains at the defect core. Starting from the initial position in Fig. 9(a), a stable O-interstitial configuration is obtained, the  $I_{\text{O}}^{\text{mid}}$ , where the interstitial O atom bonds with a middle-layer O atom, forming a Si-O-O-Si chain with one Si atom from each of the external layers, as shown in Fig. 11. From the external layer position, the  $I_{\text{O}}^{\text{ext}}$  defect is formed, where the interstitial O atom bonds with the O atom from an external-layer Si-O-Si chain and with an external-layer Si atom, as shown in Fig. 12. The  $I_{\text{O}}^{\text{ext}}$  is the more stable form of an oxygen interstitial, with a formation energy that is 2.27 eV lower than  $I_{\text{O}}^{\text{mid}}$ , as discussed below.

In both cases, the positions of the two O atoms making up the split interstitial are very nearly symmetric with respect to the original position of the O atom in the Si-O-Si chain

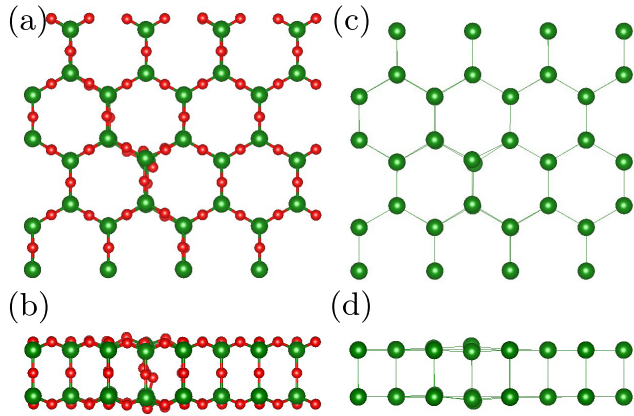


FIG. 11. Relaxed geometry of the middle-layer oxygen interstitial,  $I_{\text{O}}^{\text{mid}}$ . (a) Top and (b) side views. Si (O) atoms are shown as green (red) spheres. (c) Top and (d) side views showing only the Si honeycomb sublayers; see caption in Fig. 5.

to which the interstitial atom attaches itself. Again, in both cases the local symmetry breaking induced by the formation of the interstitials is localized in the immediate neighborhood of defect core, and involves essentially scissor and rotation modes of the O atoms in the near vicinity of the defect core, along the zigzag line of Si-O-Si bonds where the interstitial is formed. The symmetry of the Si sublattice is only disturbed at the very core of the defects, as shown in Figs. 11(c) and 11(d) and Figs. 12(c) and 12(d). More detailed views of the geometry at the core of the  $I_{\text{O}}^{\text{mid}}$  and  $I_{\text{O}}^{\text{ext}}$  are shown in Figs. SI11 and SI13 of the Supplemental Material [54].

The electronic structures of the two O interstitials are very similar. In both cases we obtain a pair of deep gap states, one in the lower half of the gap and the other in the upper half of the gap. The energies are, respectively,  $\varepsilon_{\text{vb}} + 0.91$  eV and  $\varepsilon_{\text{cb}} - 0.72$  eV, for the  $I_{\text{O}}^{\text{mid}}$ , and  $\varepsilon_{\text{vb}} + 0.65$  eV and  $\varepsilon_{\text{cb}} - 0.45$  eV for the  $I_{\text{O}}^{\text{ext}}$ . Hence, both  $I_{\text{O}}$  centers we identify are amphoteric, with deep donor and acceptor levels.

No spin splitting of the defect levels results from our spin-polarized calculations in either  $I_{\text{O}}^{\text{mid}}$  or  $I_{\text{O}}^{\text{ext}}$ . The wave functions

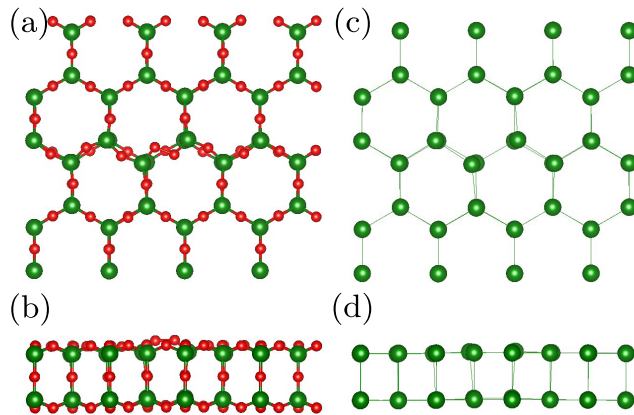


FIG. 12. Relaxed geometry of the external-layer oxygen interstitial,  $I_{\text{O}}^{\text{ext}}$ . (a) Top and (b) side views. Si (O) atoms are shown as green (red) spheres. (c) Top and (d) side views showing only the Si honeycomb sublayers; see caption in Fig. 5.

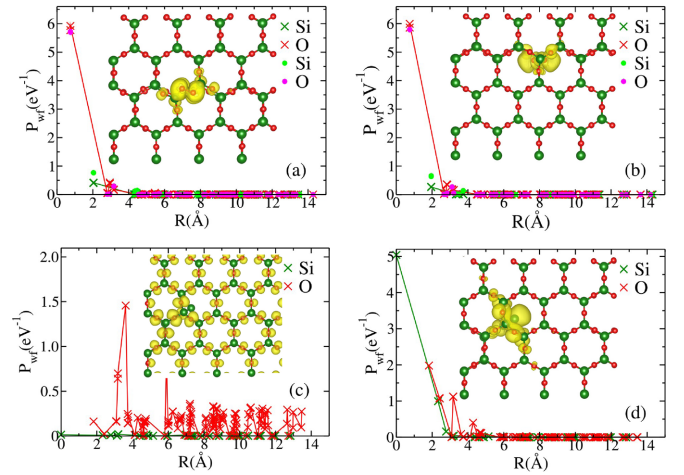


FIG. 13. (a) Wave-function spatial profile,  $P_{\text{wf}}(R)$ , of the two strongly localized gap states introduced by the external-layer oxygen interstitial,  $I_{\text{O}}^{\text{ext}}$ . The inset shows an isosurface of charge density of the state in the lower part of the gap. (b)  $P_{\text{wf}}(R)$  of the two strongly localized gap states introduced by the middle-layer oxygen interstitial,  $I_{\text{O}}^{\text{mid}}$ . The inset shows an isosurface of charge density of the state in the higher part of the gap. (c)  $P_{\text{wf}}(R)$  of the very shallow gap state at  $\varepsilon_{\text{vb}} + 0.03$  eV, introduced by the silicon interstitial,  $I_{\text{Si}}$ . The inset shows an isosurface of charge density of this shallow state. The effective-mass-theory nature of the state is displayed by a wave function that extends over the entire supercell. (d)  $P_{\text{wf}}(R)$  of the strongly localized, marginally shallow gap state at  $\varepsilon_{\text{vb}} + 0.15$  eV, introduced by  $I_{\text{Si}}$ . The inset shows an isosurface of charge density of this shallow state. In all cases, the contributions to  $P_{\text{wf}}(R)$  from Si (O) orbitals are shown as dark and light green (red and magenta) symbols and guide-to-the-eye lines.

for the two gap states, for both  $I_{\text{O}}$  species, are essentially the bonding and antibonding combinations of the O-O bond at the cores of the two  $I_{\text{O}}$  species. The orbitals in these two O atoms account for nearly the full wave function of both defect states, in each case. Figures 13(a) and 13(b) show that these are very localized deep defect states, with their wave functions decaying to zero within  $\sim 3.5$  Å from the defect center. The inset in Fig. 13(a) shows a charge-density isosurface for the  $\varepsilon_{\text{vb}} + 0.65$  eV level of  $I_{\text{O}}^{\text{ext}}$  and Fig. 13(b) shows the isosurface for the  $\varepsilon_{\text{cb}} - 0.72$  eV of  $I_{\text{O}}^{\text{mid}}$ .

## 2. Silicon interstitial: $I_{\text{Si}}$

A Si interstitial in crystalline 2D-SiO<sub>2</sub> is stable only in an interstitial site of the intermediate oxygen layer, as shown in Fig. 14, where the relaxed configuration of the  $I_{\text{Si}}$  defect is displayed. In the figure, it is observed that a Si-O bond from the pristine bilayer, between a Si atom in the top layer and the O atom in the middle layer, is replaced by a Si-Si bond between the interstitial and the top layer Si atom, while the middle-layer O atom also bonds with the Si interstitial, forming a Si-Si-O-Si chain at the core of the defect. All core atoms but the interstitial Si atom itself recover their pristine-lattice coordination.

Again, the surrounding lattice retains the symmetry of the pristine system, with symmetry reduction confined to a small region surrounding the defect core. Thus, even in this case,

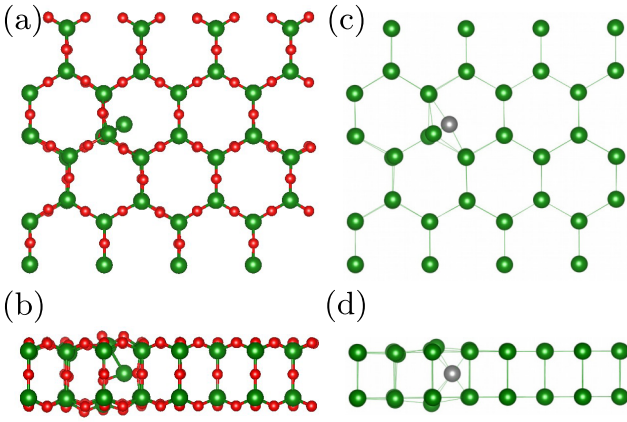


FIG. 14. Relaxed geometry of the silicon interstitial,  $I_{\text{Si}}$ . (a) Top and (b) side views. Si (O) atoms are shown as green (red) spheres. Interstitial Si atom is shown as gray sphere. (c) Top and (d) side views showing only the Si honeycomb sublayers; see caption in Fig. 5.

where a large interstitial atom is inserted in the 2D-SiO<sub>2</sub> bilayer, we observe that the lattice responds to the perturbation through scissor and rotation modes of the O atoms in the vicinity of the defect, with the external honeycomb sublattices of Si atoms being disturbed only in a very small region surrounding the defect center.

The  $I_{\text{Si}}$  is in a rather low twofold coordination, which explains a plethora of five defect-state energy levels in the band gap associated with the  $I_{\text{Si}}$  defect, as shown in Fig. 10. Unlike in the case of the Si vacancy, in the neutral charge state no spin polarization effects are observed in this case; hence the neutral  $I_{\text{Si}}$  center is EPR inactive.

Of the five  $I_{\text{Si}}$  gap states in Fig. 10, the lowest one is a very shallow level at  $\epsilon_{\text{vb}} + 0.03$  eV, which wave function is shown in Fig. 13(c). The figure clearly shows an EMT state displaying a slow decay away from the defect center, with sizable contributions to the wave function from atoms over the entire supercell, a profile that is confirmed by the charge-density isosurface in the inset. As expected, the wave function of this EMT state is dominated by the  $p$  orbitals of the external layers atoms, which is the character of the states at the top of the valence band.

Moving up in energy, in the band gap, we find a marginally shallow state at  $\epsilon_{\text{vb}} + 0.15$  eV, followed by a very deep level at  $\epsilon_{\text{vb}} + 2.23$  eV. The shallow state at  $\epsilon_{\text{vb}} + 0.15$  eV derives its wave function from atomic orbitals of the interstitial Si atom, the Si atom that bonds to it, the three middle-layer O atoms that are nearest to the interstitial Si, and the two top-layer O atoms that are nearest to the interstitial Si, as shown in Fig. 13(d). This is another example of a shallow state that is not an EMT state, being actually a very localized state with a wave function that is confined within  $\sim 3.5$  Å from the defect center.

Further up in the higher part of the gap, we find another deep level at  $\epsilon_{\text{cb}} - 0.42$  eV, and another marginally shallow level  $\epsilon_{\text{cb}} - 0.26$  eV. Overall, except for the very shallow EMT state described above, the other four gap states introduced by the  $I_{\text{Si}}$  defect are strongly localized, within  $\sim 3.5$  Å from the defect center. In particular the two marginally shallow levels, the acceptor at  $\epsilon_{\text{vb}} + 0.15$  eV and the donor at

$\epsilon_{\text{cb}} - 0.26$  eV, display strongly localized wave functions, as shown in Fig. S116 of the Supplemental Material [54]; i.e., despite being shallow states, neither is an EMT state.

## V. FORMATION ENERGY OF VACANCIES AND INTERSTITIALS

The formation energy of a neutral defect is essentially the difference between the energy of a supercell with the defect and that of a pristine supercell without the defect, taking into account the chemical potentials of each atomic species, in order to properly compare systems with different stoichiometries, as follows:

$$E_f^d = E_{\text{tot}}^d - E_{\text{tot}}^{\text{bulk}} + \sum_i n_i \mu_i, \quad (1)$$

where  $E_{\text{tot}}^d$  is the total energy of a supercell with defect  $d$ ,  $E_{\text{tot}}^{\text{bulk}}$  is the total energy of the corresponding (same supercell size) pristine bulk supercell, and  $n_i$  and  $\mu_i$  are the quantities and chemical potentials of the atoms exchanged with the corresponding chemical-potential reservoirs, when the defect is created. In the cases we consider in this work, there is only one atom exchanged with the chemical-potential reservoirs: one atom is removed from the 2D-SiO<sub>2</sub> bilayer in the case of single vacancies, and one atom is added in the case of single interstitials.

The chemical potentials of Si and O are determined by imposing a condition of thermodynamical equilibrium between the 2D-SiO<sub>2</sub> bilayer and the reservoirs of Si or O atoms employed in the synthesis of the bulk material. The 2D-SiO<sub>2</sub> bulk is obtained by electron beam deposition where a Si sample is exposed to an electron beam that heats it up, creating a vapor of silicon atoms in a gaseous O<sub>2</sub> environment [1]. The thermodynamical equilibrium condition requires

$$\mu_{\text{SiO}_2} = \mu_{\text{Si}} + \mu_{\text{O}_2} = \mu_{\text{Si}} + 2\mu_{\text{O}}, \quad (2)$$

where  $\mu_{\text{SiO}_2}$  is the calculated total energy per formula unit of a pristine SiO<sub>2</sub> bilayer. We define two limits for the synthesis: Si-rich and O-rich conditions.

In the Si-rich scenario, a gas of Si atoms in equilibrium with a bulk Si is present, and the value of  $\mu_{\text{Si}}$  is obtained from the calculated total energy per atom of diamond-lattice bulk Si. In this condition, the oxygen chemical potential is obtained from the equilibrium condition, Eq. (2), as

$$\begin{aligned} \text{Si-rich: } \mu_{\text{Si}} &= \frac{E_{\text{tot}}^{\text{Si}}}{N_{\text{Si}}}, \\ \mu_{\text{O}} &= \frac{(\mu_{\text{SiO}_2} - \mu_{\text{Si}})}{2}, \end{aligned} \quad (3)$$

where  $E_{\text{tot}}^{\text{Si}}$  is the total energy of an  $N_{\text{Si}}$ -atom Si-bulk unit cell.

On the other hand, in the O-rich scenario, the oxygen chemical potential  $\mu_{\text{O}}$  is obtained from a calculations for an O<sub>2</sub> molecular gas, and the Si chemical potential is given by the equilibrium condition, Eq. (2), as

$$\begin{aligned} \text{O-rich: } \mu_{\text{O}} &= \frac{E_{\text{tot}}^{\text{O}_2}}{2}, \\ \mu_{\text{Si}} &= (\mu_{\text{SiO}_2} - 2\mu_{\text{O}}), \end{aligned} \quad (4)$$



TABLE II. Chemical potentials of silicon and oxygen and formation energies (in eV) of neutral native defects in 2D-SiO<sub>2</sub>, for Si-rich and O-rich conditions.

	Si-rich limit (eV)	O-rich limit (eV)
$\mu_{\text{O}}$	-439.10	-434.74
$\mu_{\text{Si}}$	-245.02	-253.74
$V_{\text{O}}^{\text{mid}}$	0.59	4.95
$V_{\text{O}}^{\text{ext}}$	1.03	5.39
$V_{\text{Si}}$	13.23	4.53
$I_{\text{O}}^{\text{mid}}$	7.97	3.61
$I_{\text{O}}^{\text{ext}}$	5.70	1.34
$I_{\text{Si}}$	4.02	12.72

where  $E_{\text{tot}}^{\text{O}_2}$  is the total energy of a calculation for an O<sub>2</sub> molecule in a supercell with large vacuum regions in all three directions.

More specifically, for the the formation energy of a vacancy in the neutral charge state, from the total energy of a 2D-SiO<sub>2</sub> supercell with  $N_{\text{Si}}$  formula units and one missing O (Si) atom, we obtain

$$E_f^{V_{\text{O}}} = E_{\text{tot}}^{V_{\text{O}}} + \mu_{\text{O}} - E_{\text{tot}}^{\text{SiO}_2}(N_{\text{Si}}), \quad (5)$$

$$\begin{aligned} E_f^{V_{\text{Si}}} &= E_{\text{tot}}^{V_{\text{Si}}} + \mu_{\text{Si}} - E_{\text{tot}}^{\text{SiO}_2}(N_{\text{Si}}) \\ &= E_{\text{tot}}^{V_{\text{Si}}} + \mu_{\text{SiO}_2} - 2\mu_{\text{O}} - E_{\text{tot}}^{\text{SiO}_2}(N_{\text{Si}}), \end{aligned} \quad (6)$$

where  $E_{\text{tot}}^{\text{SiO}_2}(N_{\text{Si}})$  is the total energy of a pristine 2D-SiO<sub>2</sub> cell with  $N_{\text{Si}}$  formula units.

In the case of interstitials, we obtain

$$E_f^{I_{\text{O}}} = E_{\text{tot}}^{I_{\text{O}}} - \mu_{\text{O}} - E_{\text{tot}}^{\text{SiO}_2}(N_{\text{Si}}), \quad (7)$$

$$\begin{aligned} E_f^{I_{\text{Si}}} &= E_{\text{tot}}^{I_{\text{Si}}} - \mu_{\text{Si}} - E_{\text{tot}}^{\text{SiO}_2}(N_{\text{Si}}) \\ &= E_{\text{tot}}^{I_{\text{Si}}} - \mu_{\text{SiO}_2} + 2\mu_{\text{O}} - E_{\text{tot}}^{\text{SiO}_2}(N_{\text{Si}}). \end{aligned} \quad (8)$$

The values we obtain for  $\mu_{\text{Si}}$  and  $\mu_{\text{O}}$  in the two limits are included in Table II. The table also includes the values of  $E_f$  in the two limits for all native defects we consider, and Fig. 15 shows  $E_f$  as a function of  $\mu_{\text{O}}$  over the chemical potential range between the Si-rich and O-rich limits. The results in Table II show that while oxygen vacancies are more stable in the intermediate layer of O atoms than in the external layers, by 0.44 eV, the opposite is true for the oxygen interstitials, which are much more stable in the external layer, by 2.27 eV, than in the intermediate layer.

Figure 15 and Table II show that the  $V_{\text{O}}^{\text{mid}}$  vacancy is the most stable defect over the first three-fifths of the range of chemical potentials we consider, starting from the Si-rich limit, and that the  $I_{\text{O}}^{\text{ext}}$  becomes the most stable defect from there up to the O-rich limit. These trends are expected, since in O-poor conditions we expect higher concentration of O vacancies and in O-rich conditions we expect higher concentrations of O interstitials, but the intervals of chemical potential values where each of these two defect species are stable must be determined from calculations such as presented here.

Another non-straightforward conclusion from our calculations is that in O-rich conditions, hence Si-poor conditions

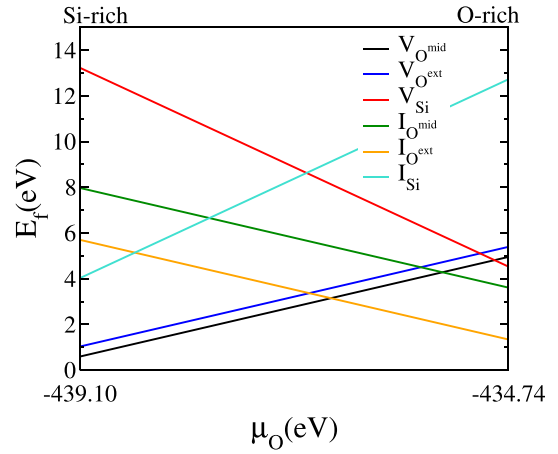


FIG. 15. Formation energy,  $E_f$ , as a function of the oxygen chemical potential,  $\mu_{\text{O}}$ , for the six defect species considered in this work.  $\mu_{\text{O}}$  values range from a Si-rich value on the left up to an O-rich value on the right, as explained in the text.

(given the SiO<sub>2</sub>-bulk thermodynamical constraint on the sum of chemical potentials), O interstitials are more abundant than Si vacancies, and in O-poor conditions, hence Si-rich conditions, O vacancies are more abundant than Si interstitials. Note that in the Si-rich limit of chemical potentials we consider, the  $E_f$  values of the oxygen vacancies are much smaller (by at least 3 eV) than that of the silicon interstitial. Similar considerations apply in the O-rich limit, where  $E_f$  for the  $I_{\text{O}}^{\text{ext}}$  interstitial is smaller than  $E_f$  for the silicon vacancy by 4.2 eV.

To summarize, among the single native defects we consider, oxygen native defects are expected to be the most abundant species in thermal equilibrated samples under the synthesis conditions encode in our choices of chemical potentials.

In the Supplemental Material [54], for each native defect in our study, we include figures with detailed views of the atomic structure at the core of the defect, as well larger and more detailed figures of the DOS plots, the wave-function spatial profiles, and isosurfaces of charge density of the defect states we discuss above. We also include a detailed explanation of the definition of the wave-function spatial profile and the atomic cartesian coordinates of all defect supercells we employed in our calculations.

## VI. CONCLUSIONS

Structural and electronic properties of single O and Si vacancies, and single O and Si interstitials in a 2D-SiO<sub>2</sub> bilayer, were addressed in this work. In general, our results indicate that oxygen native defects should be the most abundant defect species in thermal equilibrated samples, for the range of chemical potentials we have considered. While oxygen vacancies in the middle layer are more stable than in the external layers by 0.44 eV, the opposite is true for oxygen interstitials, which are more stable in the external layer, by a large 2.27 eV energy difference, than in the middle layer. Overall, the middle-layer oxygen vacancy is the most stable defect over the first three-fifths of the range of chemical potentials we consider, starting from the Si-rich limit, and the external-layer

oxygen interstitial becomes the most stable defect from there up to the O-rich limit.

Our results allow us to identify scissor and rotation modes of displacements of oxygen atoms in the Si-O-Si chains, that are low-energy structural excitations of the 2D-SiO<sub>2</sub> lattice, and constitute the dominant mechanism by which the 2D-SiO<sub>2</sub> lattice responds to the formation of all native defects in the present study. In all cases, the structure of the two honeycomb sublattices of Si atoms remain nearly unaffected by the presence of the defects, except in the very near vicinity of the defect core.

Our calculations for the electronic structure of the pristine bulk of 2D-SiO<sub>2</sub> reveal the emergence of a very strong van Hove singularity at  $-1.73$  eV below the top of the valence band, associated with a set of flat bands in this energy range, that should give rise to a strong peak in the ultraviolet absorption signal of a 2D-SiO<sub>2</sub> layer. No such strong electronic singularity is observed in the 3D forms of 3D-SiO<sub>2</sub>.

Regarding the electronic states associated with these native defects in the fundamental band gap, a general trend we have identified is a strong tendency, for all native defect we consider, for the formation of strongly localized defect levels, regardless of whether their energies are shallow or deep

within the band gap. We have also identified a tendency for the formation of localized states that are resonant within the bulk bands, near the edges of the valence and/or conduction bands.

Oxygen monovacancies and single interstitials are found to be amphoteric trapping centers in 2D-SiO<sub>2</sub>, displaying acceptor and donor levels in the fundamental band gap of 2D-SiO<sub>2</sub>. Both silicon native defects we have considered introduce several strongly localized states spanning a large fraction of the gap.

Our results indicate that in 2D-SiO<sub>2</sub>, even shallow defect states exhibit strongly localized wave functions. We expect trapping and polaronic effects to be a feature of defect states in 2D-SiO<sub>2</sub>, as a result of quantum confinement and enhanced Coulombic effects in this 2D system.

## ACKNOWLEDGMENTS

We acknowledge funding from the Brazilian funding agencies Conselho Nacional de Desenvolvimento Científico e Tecnológico (CNPq), Coordenação de Aperfeiçoamento de Pessoal de Nível Superior (CAPES), and Fundação de Amparo à Pesquisa do Estado de Minas Gerais (FAPEMIG), Brazilian Institute of Science and Technology in Carbon Nanomaterials (INCT)-Nanocarbono.

- 
- [1] K. Büchner and M. Heyde, *Prog. Surf. Sci.* **92**, 341 (2017).
- [2] L. Lichtenstein, C. Büchner, B. Yang, S. Shaikhutdinov, M. Heyde, M. Sierka, R. Włodarczyk, J. Sauer, and H.-J. Freund, *Angew. Chem., Int. Ed.* **51**, 404 (2012).
- [3] M. Heyde, S. Shaikhutdinov, and H.-J. Freund, *Chem. Phys. Lett.* **550**, 1 (2012).
- [4] C. Büchner, L. Lichtenstein, X. Yu, J. Boscoboinik, B. Yang, W. Kaden, M. Heyde, S. Shaikhutdinov, R. Włodarczyk, M. Sierka, J. Sauer, and H.-J. Freund, *Chem. - Eur. J.* **20**, 9176 (2014).
- [5] C. Büchner, Z. J. Wang, K. Burson, M.-G. Willinger, M. Heyde, R. Schlögl, and H.-J. Freund, *ACS Nano* **10**, 7982 (2016).
- [6] R. Weeks, *J. Appl. Phys.* **27**, 1376 (1956).
- [7] M. Stapelbroek Jr., D. Griscom, E. Friebele, and G. Sigel, *J. Non-Cryst. Solids* **32**, 313 (1979).
- [8] D. Griscom, *J. Non-Cryst. Solids* **149**, 137 (1992).
- [9] J. Götze, Y. Pan, and A. Müller, *Mineral. Mag.* **85**, 639 (2021).
- [10] Z. Y. Lu, C. J. Nicklaw, D. M. Fleetwood, R. D. Schrimpf, and S. T. Pantelides, *Phys. Rev. Lett.* **89**, 285505 (2002).
- [11] N. Richard, L. Martin-Samos, G. Roma, Y. Limone, and J. Crocombette, *J. Non-Cryst. Solids* **351**, 1825 (2005).
- [12] L. Martin-Samos, Y. Limoge, J. P. Crocombette, G. Roma, N. Richard, E. Anglada, and E. Artacho, *Phys. Rev. B* **71**, 014116 (2005).
- [13] R. Sahl, in *Crystalline Silicon* (IntechOpen, London, 2011), pp. 135–172.
- [14] A. El-Sayed, K. Tanimura, and A. Shluger, *J. Phys.: Condens. Matter* **27**, 265501 (2015).
- [15] D. Griscom, D. Brown, and N. Saks, *The Physics and Chemistry of SiO<sub>2</sub> and the Si-SiO<sub>2</sub> Interface* (Springer, New York, 1988), pp. 287–297.
- [16] M. Boero, A. Pasquarello, J. Sarnthein, and R. Car, *Phys. Rev. Lett.* **78**, 887 (1997).
- [17] L. Giacomazzi, L. Martin-Samos, A. Boukenter, Y. Ouerdale, S. Girard, and N. Richard, *Phys. Rev. B* **90**, 014108 (2014).
- [18] L. Giacomazzi, L. Martin-Samos, A. Boukenter, Y. Ouerdane, S. Girard, A. Alessi, S. de Gironcoli, and N. Richard, *Nanotechnology* **28**, 195202 (2017).
- [19] J. Götze, M. Plötze, H. Fuchs, and D. Haberman, *Mineral. Mag.* **63**, 149 (1999).
- [20] J. Götze, Y. Pan, M. Stevens-Kalceff, U. Kempe, and A. Müller, *Am. Mineral.* **100**, 1469 (2015).
- [21] J. Götze, R. Möckel, and Y. Pan, *Minerals* **10**, 1037 (2020).
- [22] A. M. El-Sayed, M. B. Watkins, V. V. Afanas, and A. L. Shluger, *Phys. Rev. B* **89**, 125201 (2014).
- [23] G. Pacchioni and A. Basile, *J. Non-Cryst. Solids* **254**, 17 (1999).
- [24] D. Y. Qiu, F. H. da Jornada, and S. G. Louie, *Phys. Rev. Lett.* **111**, 216805 (2013).
- [25] M. Ugeda, A. Bradley, S. Shi, F. da Jornada, Y. Zhang, D. Qui, W. Ruan, S. Mo, Z. Hussain, Z. Shen, F. Wang, S. Louie, and M. Crommie, *Nat. Mater.* **13**, 1091 (2014).
- [26] T. Björkman, S. Kurasch, O. Lehtinen, J. Kotakoski, O. Yazyev, A. Srivastava, V. Skakalova, J. Smet, U. Kaiser, and A. Krasheninnikov, *Sci. Rep.* **3**, 3482 (2013).
- [27] J. da Silva Araújo and R. W. Nunes, *Phys. Rev. B* **81**, 073408 (2010).
- [28] J. da Silva-Araújo, H. Chacham, and R. W. Nunes, *Phys. Rev. B* **81**, 193405 (2010).
- [29] J. da Silva-Araújo, A. J. M. Nascimento, H. Chacham, and R. W. Nunes, *Nanotechnology* **24**, 035708 (2013).
- [30] W. A. Diery, A. J. M. Moujaes, Elie A., and R. W. Nunes, *Carbon* **140**, 250 (2018).
- [31] S. S. Alexandre and R. W. Nunes, *Phys. Rev. B* **96**, 075445 (2017).

- [32] J. Soler, E. Artacho, J. Gale, A. García, J. Junquera, P. Ordejón, and D. Sánchez-Portal, *J. Phys.: Condens. Matter* **14**, 2745 (2002).
- [33] P. Hohenberg and W. Kohn, *Phys. Rev.* **136**, B864 (1964).
- [34] W. Kohn and L. Sham, *Phys. Rev.* **140**, A1133 (1965).
- [35] J. P. Perdew, K. K. Burke, and M. M. Ernzerhof, *Phys. Rev. Lett.* **77**, 3865 (1996).
- [36] D. Han, D. West, X. B. Li, S. Y. Xie, H. B. Sun, and S. B. Zhang, *Phys. Rev. B* **82**, 155132 (2010).
- [37] A. J. M. Nascimento and R. W. Nunes, *Nanotechnology* **24**, 435707 (2013).
- [38] P. K. Roy and A. Heuer, *Phys. Rev. Lett.* **122**, 016104 (2019).
- [39] P. Roy and A. Heuer, *J. Phys.: Condens. Matter* **31**, 225703 (2019).
- [40] P. Roy, M. Heyde, and A. Heuer, *Phys. Chem. Chem. Phys.* **20**, 14725 (2018).
- [41] D. Ormrod Morley, P. Salmon, and M. Wilson, *J. Chem. Phys.* **154**, 124109 (2021).
- [42] M. Wilson, A. Kumar, D. Sherrington, and M. Thorpe, *Phys. Rev. B* **87**, 214108 (2013).
- [43] H. Monkhorst and J. Pack, *Phys. Rev. B* **13**, 5188 (1976).
- [44] D. Löffler, J. J. Uhlrich, M. Baron, B. Yang, L. Lichtenstein, L. Heinke, C. Büchner, M. Heyde, S. Shaikhutdinov, H. J. Freund, R. Włodarczyk, M. Sierka, and J. Sauer, *Phys. Rev. Lett.* **105**, 146104 (2010).
- [45] N. Troullier and J. L. Martins, *Phys. Rev. B* **43**, 1993 (1991).
- [46] The quantity we call the wave-function spatial profile [ $P_{\text{wf}}(R)$ ], as defined in the Supplemental Material [54], is just another way to postprocess the electronic-structure numerical data contained in the output DOS and PDOS files generated by the *ab initio* program.
- [47] L. Lichtenstein, M. Heyde, and H.-J. Freund, *J. Phys. Chem. C* **116**, 20426 (2012).
- [48] L. Lichtenstein, The structure of two-dimensional vitreous silica, Ph.D. thesis, Freien Universität Berlin, 2012.
- [49] N. Binggeli, N. Troullier, J. L. Martins, and J. Chelikowsky, *Phys. Rev. B* **44**, 4771 (1991).
- [50] K. F. Mak, C. Lee, J. Hone, J. Shan, and T. F. Heinz, *Phys. Rev. Lett.* **105**, 136805 (2010).
- [51] Y. Zhang, T. Chang, B. Zhou, Y. Cui, H. Yan, Z. Liu, F. Schmidt, J. Lee, R. Moore, Y. Chen, H. Lin, H. Jeng, S. Mo, Z. Hussain, A. Bansil, and Z. Shen, *Nat. Nanotechnol.* **9**, 111 (2014).
- [52] E. Altman and U. Schwarz, *Adv. Mater. Interfaces* **1**, 1400108 (2014).
- [53] H. Malekpour, P. Ramnani, S. Srinivasan, G. Balasubramanian, D. Nika, A. Mulchandani, R. Lake, and A. Balandin, *Nanoscale* **8**, 14608 (2016).
- [54] See Supplemental Material at <http://link.aps.org/supplemental/10.1103/PhysRevB.106.155416> for detailed explanation of our scheme to analyze the spatial structure of the defect-state wave functions, enlarged figures of density of states plots, detailed geometry of the defect cores, enlarged figures showing the resonances and gap states generated by the defects, and the atomic-coordinate sets for all supercells in our study.